Cellular/Molecular

A Role for KCNQ Channels on Cell Type-Specific Plasticity in Mouse Auditory Cortex after Peripheral Damage

Amanda Henton,[1,2] Yanjun Zhao,[1] and ⬤Thanos Tzounopoulos[1]

[1]Pittsburgh Hearing Research Center and Department of Otolaryngology, University of Pittsburgh, Pittsburgh, Pennsylvania 15261, and [2]Center for Neuroscience, University of Pittsburgh, University of Pittsburgh, Pittsburgh, Pennsylvania 15261

Damage to sensory organs triggers compensatory plasticity mechanisms in sensory cortices. These plasticity mechanisms result in restored cortical responses, despite reduced peripheral input, and contribute to the remarkable recovery of perceptual detection thresholds to sensory stimuli. Overall, peripheral damage is associated with a reduction of cortical GABAergic inhibition; however, less is known about changes in intrinsic properties and the underlying biophysical mechanisms. To study these mechanisms, we used a model of noise-induced peripheral damage in male and female mice. We uncovered a rapid, cell type-specific reduction in the intrinsic excitability of parvalbumin-expressing neurons (PVs) in layer (L) 2/3 of auditory cortex. No changes in the intrinsic excitability of either L2/3 somatostatin-expressing or L2/3 principal neurons (PNs) were observed. The decrease in L2/3 PV excitability was observed 1, but not 7, d after noise exposure, and was evidenced by a hyperpolarization of the resting membrane potential, depolarization of the action potential threshold, and reduction in firing frequency in response to depolarizing current. To uncover the underlying biophysical mechanisms, we recorded potassium currents. We found an increase in KCNQ potassium channel activity in L2/3 PVs of auditory cortex 1 d after noise exposure, associated with a hyperpolarizing shift in the minimal voltage activation of KCNQ channels. This increase contributes to the decreased intrinsic excitability of PVs. Our results highlight cell-type- and channel-specific mechanisms of plasticity after noise-induced hearing loss and will aid in understanding the pathologic processes involved in hearing loss and hearing loss-related disorders, such as tinnitus and hyperacusis.

Key words: auditory cortex; cortical plasticity; hearing loss; intrinsic plasticity; KCNQ potassium channels

---

Significance Statement

Noise-induced damage to the peripheral auditory system triggers central plasticity that compensates for the reduced peripheral input. The mechanisms of this plasticity are not fully understood. In the auditory cortex, this plasticity likely contributes to the recovery of sound-evoked responses and perceptual hearing thresholds. Importantly, other functional aspects of hearing do not recover, and peripheral damage may also lead to maladaptive plasticity-related disorders, such as tinnitus and hyperacusis. Here, after noise-induced peripheral damage, we highlight a rapid, transient, and cell type-specific reduction in the excitability of layer 2/3 parvalbumin-expressing neurons, which is due, at least in part, to increased KCNQ potassium channel activity. These studies may highlight novel strategies for enhancing perceptual recovery after hearing loss and mitigating hyperacusis and tinnitus.

Introduction

In all sensory systems, damage to sensory organs or sensory deprivation lead to compensatory cortical reorganization and increased slope of input-output cortical response functions (gain) (Rasmusson, 1982; Merzenich et al., 1983; Robertson and Irvine, 1989; Kaas et al., 1990; Gilbert and Wiesel, 1992). Specifically, after monocular deprivation, whisker plucking, or cochlear damage, visual, somatosensory, and auditory cortices adapt to restore spontaneous and sensory-evoked responses (Qiu et al., 2000; Chambers et al., 2016), despite the reduction in peripheral input into the brain. This recovery is associated with increased cortical gain to the spared sensory input, which, in turn, is associated with robust intrinsic and synaptic cortical plasticity mechanisms. Importantly, this plasticity is consistent with a remarkable recovery in the perceptual detection thresholds of sensory stimuli (Kuhlman et al., 2013; Chambers et al., 2016). Perceptual and processing recovery are also associated with subcortical plasticity mechanisms

(Auerbach et al., 2014; Henton and Tzounopoulos, 2021), which will not be studied here. Despite the importance of cortical plasticity for the recovery of cortical responses to sensory stimuli and sensory perception after peripheral damage, the precise mechanisms by which this plasticity is achieved are not fully understood.

In this study, we investigated plasticity mechanisms in the auditory cortex (AC) after noise-induced cochlea damage. Cochlear injury leads to reduced and/or degraded input to the ascending auditory system. This peripheral damage is associated with several physiological changes in AC, such as reduced inhibitory (GABAergic) cortical activity, increased spontaneous firing, enhanced excitatory gain, and reorganization of frequency tuning toward less damaged regions of the cochlea (Seki and Eggermont, 2003; Kotak et al., 2005; Sarro et al., 2008; Scholl and Wehr, 2008; Yang et al., 2011; Takesian et al., 2013; Chambers et al., 2016; Resnik and Polley, 2017). Although this plasticity likely contributes to a remarkable recovery of perceptual sound detection (Chambers et al., 2016; Resnik and Polley, 2021), it does not fully restore other major aspects of hearing. Namely, perceptual thresholds recover when sound is presented in quiet but not noisy backgrounds (Chambers et al., 2016; Resnik and Polley, 2021). Moreover, perceptual capabilities that depend on the temporal pattern of spiking activity, such as speech, modulated noise, and complex sound discrimination, are not supported, thus preventing a full recovery of hearing (Chambers et al., 2016; X. Wang, 2016; Resnik and Polley, 2021). Finally, although this plasticity is generally adaptive, it may become maladaptive and lead to pathologic hyperexcitability, as observed in tinnitus and hyperacusis (Auerbach et al., 2014; Henton and Tzounopoulos, 2021). Therefore, investigation of the synaptic and intrinsic mechanisms underlying this plasticity holds the promise to highlight novel strategies for enhancing perceptual recovery after hearing loss and mitigating brain plasticity-related disorders, such as hyperacusis and tinnitus.

In the AC, after peripheral injury, excitatory postsynaptic responses are increased in glutamatergic excitatory principal neurons (PNs), whereas GABAergic inhibitory responses are decreased (Kotak et al., 2005; Yang et al., 2011, 2012; W. Wang et al., 2019). In terms of intrinsic properties, 10-12 d after peripheral damage, PNs display increased excitability (Yang et al., 2012), whereas parvalbumin-expressing inhibitory interneurons (PVs) display decreased firing rate after sustained stimulation (W. Wang et al., 2022). Although these studies highlight the important role of cortical intrinsic plasticity after cochlear damage, the underlying changes in channel activity, the cell-type specificity, and the time course of intrinsic plasticity remain unknown. To elucidate these mechanisms in AC, we used a mouse model of noise-induced cochlear damage, in combination with cell type-specific labeling and *ex vivo* electrophysiology techniques. Our results reveal a time-dependent and cell type-specific scheme of intrinsic plasticity that involves precise changes in the biophysical properties of KCNQ channels.

Materials and Methods

Animals. Male and female PV-Cre-Ai14, SOM-GFP, and C57BL/6 (C57) mice were used for all experiments. Maturation of synaptic and intrinsic properties of cortical neurons is completed by P30 (Metherate and Aramakis, 1999; Oswald and Reyes, 2008; Froemke and Jones, 2011; Kinnischtzke et al., 2012; Miyamae et al., 2017). To ensure that no developmental differences affect baseline cellular and synaptic properties, experimental procedures started in mice that were older than P30 and were completed by P55 (P31-P55). Experiments and analyses were performed with the experimenter blind to the exposure condition. All

experimental procedures were approved by the University of Pittsburgh Animal Care and Use Committee.

Stereotaxic injections. Mice were anesthetized with isoflurane (3% induction, 1.5% maintenance) and secured to a stereotaxic frame (Kopf); respiration and body temperature were monitored throughout the procedure. To label L5 projection neurons and localize AC for acute slice recordings, we injected green retrograde fluorescent latex microspheres (retrobeads) (Lumafluor) in the right inferior colliculus, as done previously (Joshi et al., 2015). Briefly, a small craniotomy was drilled 1 mm posterior and 1 mm lateral to λ, at an injection depth of 0.75 mm. Retrobeads ($\sim$0.1 µl) were pressure injected (Picospritzer, 25 psi, 12-15 ms duration) into the right inferior colliculus. To retrogradely label cortical projection neurons in the contralateral (right) AC (see Fig. 1), a small craniotomy was drilled into the left AC (4 mm posterior, 4 mm lateral to bregma) and $\sim$0.1 µl of red retrobeads was injected at a depth of 1 mm. Injection pipettes were left in the brain for 2 min before withdrawing. Mice were allowed to recover for a minimum of 2 d before any experimental procedures.

Auditory brainstem response (ABR) and noise exposure (NE). ABRs were measured immediately before sham or NE, and 1 or 7 d after exposure (right before the electrophysiological recordings assessing cellular excitability in the AC). Mice were anesthetized with 1.5% isoflurane and placed on an electric heating pad in a sound-attenuated recording chamber (Med Associates). Although isoflurane affects ABR thresholds (Cederholm et al., 2012; Ruebhausen et al., 2012; Thiele and Köppl, 2018), in all experiments both noise- and sham- exposed mice were anesthetized using isoflurane. Thus, the use of isoflurane does not affect the conclusions of our study. A 200 µl pipette tip was inserted to the end of a plastic tube attached to a closed field speaker (CF-1, Tucker Davis Technologies) and was then inserted into the left ear. The total length from the speaker to the tip of the pipette was $\sim$4.45 cm. Stimulus presentation and data acquisition were controlled by the Tucker Davis Technologies Rz6 System 3 software. Stimuli presented included 10, 16, 20, 24, and 32 kHz frequencies. The rise-fall time of the tone pips was 1.5 ms. Evoked responses were averaged over 512 trials. Calibration for ABR tone delivery was conducted via a 1/8 inch microphone amplifier (4954-B, Bruel & Kjaer) affixed to the end of the pipette tip used for tone delivery. The TDT program SigCal was used to calibrate the amplitude for each tone used. ABR thresholds were analyzed in a blind fashion by one observer, and an additional independent reviewer assessed thresholds in a blind fashion: the results we obtained were similar. Threshold was defined as the lowest stimulus intensity that produced a Wave 1 response. A Wave 1 response waveform is identified, and distinguished from nonresponse (noise), as the first consistent wave generated with decreased amplitude and increased latency as the stimulus intensity decreases. For NE, mice were anesthetized with isoflurane (1.5%) and a pipette was fixed to a speaker (MF-1; Tucker Davis Technologies) and then inserted into the left ear. The speaker was calibrated with a 1/4-inch microphone (4954-B, Bruel & Kjaer) using a 1 kHz, 94 dB SPL sound calibrator standard (Type 4231, Bruel & Kjaer). Mice were unilaterally exposed to an 8-16 kHz sound at 116 dB SPL for 1 h. Sham mice underwent the same ABR and exposure protocol, without the presentation of noise.

Brain slice electrophysiology. Experimental mice were deeply anesthetized with isoflurane before dissection and preparation of acute mouse brain slices (300 µm) containing the AC. Ice-cold sucrose cutting solution was used and contained the following in (mM): 2.5 KCl, 1.25 NaH$_2$PO$_4$, 25 NaHCO$_3$, 0.5 CaCl$_2$, 7 MgCl$_2$, 7 dextrose, 205 sucrose, 1.3 ascorbic acid, and 3 sodium pyruvate (bubbled with 95% O$_2$/5% CO$_2$, pH $\sim$ 7.25-7.35). Slices were then transferred and incubated in a chamber at 36°C for 30 min in aCSF containing the following (in mM): 125 NaCl, 2.5 KCl, 1.25 NaH$_2$PO$_4$, 25 NaHCO$_3$, 2 CaCl$_2$, 1 MgCl$_2$, 10 glucose, 1.3 ascorbic acid, and 3 sodium pyruvate (bubbled with 95% O$_2$/5% CO$_2$). After a 30 min incubation, slices were maintained at room temperature before recordings. For measurements of intrinsic excitability and membrane properties (see Figs. 2-4), the bath solution was identical to the incubation solution and was maintained at 32°C-34°C with an inline heating system (Warner TC324-B). To isolate intrinsic properties, the following synaptic blockers were added to the bath solution (in mM): 0.01 DNQX (HelloBio), 0.05 APV (HelloBio), and 0.03 gabazine

(HelloBio), to block AMPA, NMDA, and $GABA_A$ receptors, respectively. Borosilicate patch pipettes (ID: 1.1 mm, OD: 1.5 mm, Sutter Instruments) were pulled into patch electrodes with 3-5 MΩ resistance and filled with a potassium-based intracellular solution, containing the following (in mM): 128 K-gluconate, 10 HEPES, 4 $MgCl_2$, 4 Na_2ATP, 0.3 Tris-GTP, 10 Tris phosphocreatine, 1 EGTA, and 3 sodium ascorbate (pH 7.20-7.25 and 290-300 mOsmol). Series resistance (R_{series}) was determined by delivering a −5 mV voltage step (command potential set at −70 mV) and dividing the −5 mV voltage step by the peak current generated. Input resistance (R_{input}) was determined by delivering the same −5 mV step and measuring the difference between the baseline and steady-state hyperpolarized current (ΔI) and was calculated using the following formula: $R_{input} = -5\,mV/\Delta I - R_{series}$. For intrinsic property experiments (see Figs. 2-4), cells with R_{series} >25 MΩ were discarded. For our R_{series} criteria on potassium current experiments, see subsequent sections. For all experiments, both R_{series} and R_{input} were monitored throughout the experiment: we discarded cells that showed a change >20% in either R_{series} or R_{input} during the experiment. Pipette capacitance was compensated. Data were sampled at 10 kHz and Bessel filtered at 4 kHz. Resting membrane potential was measured in voltage-follower mode (current-clamp, at $I = 0$), 30-60 s after breaking in and averaged over 30 s. To assess action potential (AP) properties, we delivered a series of depolarizing current steps from −100 to 400 pA. AP properties were analyzed from the first resulting AP at rheobase. AP width was calculated as the FWHM amplitude of the AP. The AP threshold was measured in phase plane, as the membrane potential at which the depolarization slope exhibited the first abrupt change (Δslope > 10 V/s). AP height was measured as the difference between the AP threshold and the AP peak. AP latency was measured as the time between stimulus onset and the peak of the first AP.

Sustained delayed-rectifier potassium current recordings. To record sustained delayed-rectifier potassium currents, a low Ca^{2+} (0.5 mM) external solution was used, and the internal solution was identical to that used in previously described recordings but with the addition of 5 mM BAPTA to minimize Ca^{2+}-activated potassium currents. The bath solution contained the following blockers (in mM): 0.05 APV (NMDARs), 0.01 DNQX (AMPARs), 0.03 gabazine ($GABA_ARs$), 0.1 saclofen ($GABA_BRs$), 0.1 (μm) TTX (Na^+ channels), 0.01 XE-991 (KCNQ channels), and 0.1 ZD2788 (HCN channels). We corrected for the liquid junction potential (−12 mV) (see Fig. 5). Whole-cell capacitance and series resistance were compensated 60%-70% at 4 kHz bandwidth after compensation, and cells with residual R_{series} that was >7.5 MΩ were discarded. The mean residual R_{series} values were 6.89 ± 0.814 MΩ for sham-exposure and 7.02 ± 0.91 MΩ for noise-exposure experiments, and were not significantly different ($p = 0.73$, unpaired t test). Cells were held at −70 mV before delivering 300 ms depolarizing steps (−70 to −10 mV, 10 mV increments). Hyperpolarizing pulses (from −100 mV to −80 mV, in 5 mV increments) were delivered to measure linear leak currents that were then extrapolated to the depolarizing steps and subtracted from the recorded currents elicited from the protocol shown in Figure 5A. Average current amplitude was measured from the last 100 ms of the 300 ms depolarizing pulse, as A-type potassium currents rapidly deactivate at 50 ms.

I_A *transient potassium current recordings.* A-type potassium currents (I_A) were isolated by extracellular application of the following blockers (in mM): 0.05 APV, 0.01 DNQX, 0.1 saclofen, 0.03 gabazine, 0.1 (μm) TTX, and 20 TEA (delayed rectifier K^+ channel blocker). Moreover, low Ca^{2+} (0.5 mM) external solution was used, and the internal solution was identical to that used in previously described recordings, and included 5 mM BAPTA to minimize Ca^{2+}-activated potassium currents. The liquid junction potential (−12 mV) was corrected (see Fig. 5). Whole-cell capacitance and R_{series} were compensated 60%-70% at 4 kHz bandwidth. After compensation, cells with a residual R_{series} that was >7.5 MΩ were discarded. The mean residual R_{series} values were 6.78 ± 0.69 MΩ for sham-exposure and 6.59 ± 0.88 MΩ for noise-exposure experiments, and were not significantly different ($p = 0.69$, unpaired t test). Cells were held at −100 mV between stimulus presentations to allow recovery from inactivation, and the interstimulus interval was 2.5 s. On interleaved trials, either −70 or −40 mV voltage steps were presented before stepping the voltage to 0 mV for 300 ms. Since I_A currents are inactivated at −40 mV, this sweep was subtracted from the −70 mV sweep to isolate I_A. Charge of

I_A was calculated as the integrated current over the first 25 ms of stimulus presentation.

KCNQ potassium current recordings. For KCNQ voltage-clamp recordings (see Fig. 7), the same internal solution was used as in Figures 2-4. KH_2PO_4-free external solution was used for KCNQ recordings to avoid precipitation with $CsCl_2$ (1 mm) and $CdCl_2$ (200 μM), which were added to block HCN and calcium channels. DNQX, gabazine, and TTX were also added to the bath. The measured liquid junction potential (−12 mV) was corrected. Whole-cell capacitance and R_{series} were compensated 60%-70% at 4 kHz bandwidth. After compensation, cells with a residual R_{series} >7.5 MΩ were discarded. The mean residual R_{series} values were 6.57 ± 0.79 MΩ for sham-exposure and 6.79 ± 0.71 MΩ for noise-exposure experiments, and were not significantly different ($p = 0.57$, unpaired t test). To measure KCNQ currents in L2/3 PVs in AC, we held PVs at −30 mV for 5 s and then stepped the voltage to −50 mV for 1 s to reveal the slowly deactivated current. To find the XE-991-sensitive KCNQ current, we applied 10 μM XE-991 and recorded the remaining current. The XE-991-remaining current was subtracted from the control current to calculate the KCNQ current.

To measure the voltage activation threshold of KCNQ channels, slow voltage ramps (10 mV/s) were delivered from −70 to −10 mV. This voltage protocol reveals an outward current that is partially blocked by the KCNQ channel blocker XE-991 (10 μM; HelloBio). XE-991 was added to the bath solution for at least 15 min before repeating the voltage ramp protocol. XE-991 current was subtracted from the baseline current to reveal the XE-991-sensitive current, KCNQ current. We corrected for the remaining series resistance after compensation using the following formula: Vm = Vcmd − (Im × residual R_{series}). We then interpolated to a common voltage curve (using an interpolation function in MATLAB), and then subtracted the XE-991-sensitive curve from the control current to reveal the XE-99-sensitive KCNQ current. To calculate the threshold voltage of activation, we measured at what voltage the current increased >4 SDs from the mean baseline current. For cells to be included in this analysis, the residual R_{series} had to be <7.5 MΩ, so that we were able to interpolate to a common voltage scale between experimental conditions at least to −50 mV. The mean residual R_{series} values were 5.69 ± 0.75 MΩ for sham-exposure and 5.23 ± 1.03 MΩ for noise-exposure experiments, and were not significantly different ($p = 0.55$, unpaired t test).

Data analysis and statistics. Statistical analyses were performed in Prism 9 (GraphPad). For two-sample comparisons, unpaired t tests were used for between-subject data (see Figs. 5, 7). For comparison between multiple groups of normally distributed data, two-way ANOVA test was used (see Figs. 2-4); non-normally distributed data were log-transformed (see Fig. 4M). For comparisons between multiple groups having within-subject factors, a repeated-measures two-way ANOVA was used for normally distributed data populations and Friedman test for non-normally distribution (see Fig. 6). Normality was determined using the Shapiro–Wilk normality test. We used three-way ANOVA for comparisons between groups to assess the effects of exposure, time, and frequency in ABR measurements (see Fig. 1), and in f-I curves (see Fig. 6A,C) to assess the effects of exposure, drug, and current. Non-normally distributed data were analyzed using the Friedman nonparametric statistical test (see Fig. 6B,D). Bonferroni or Tukey multiple comparison *post hoc* tests were used after ANOVA. For detailed values and statistical tests for all figures, see Tables 1-3. Group data are presented as mean ± SEM.

Results

To cause noise-induced hearing loss (peripheral damage), we unilaterally exposed mice to an 8-16 kHz, 116 dB SPL loud sound 1 h (Fig. 1A). As control, we used sham-exposed (SE) mice, which underwent identical procedures but without the presentation of sound. To assess and quantify the effect of our NE protocol on peripheral function, we used ABR measurements, which measure the synchronous activity of the auditory nerve and auditory brainstem nuclei from the cochlea to the inferior colliculus, in response to acoustic stimuli. ABRs were recorded immediately before NE or SE and then again at 1 and 7 d after exposure. NE,
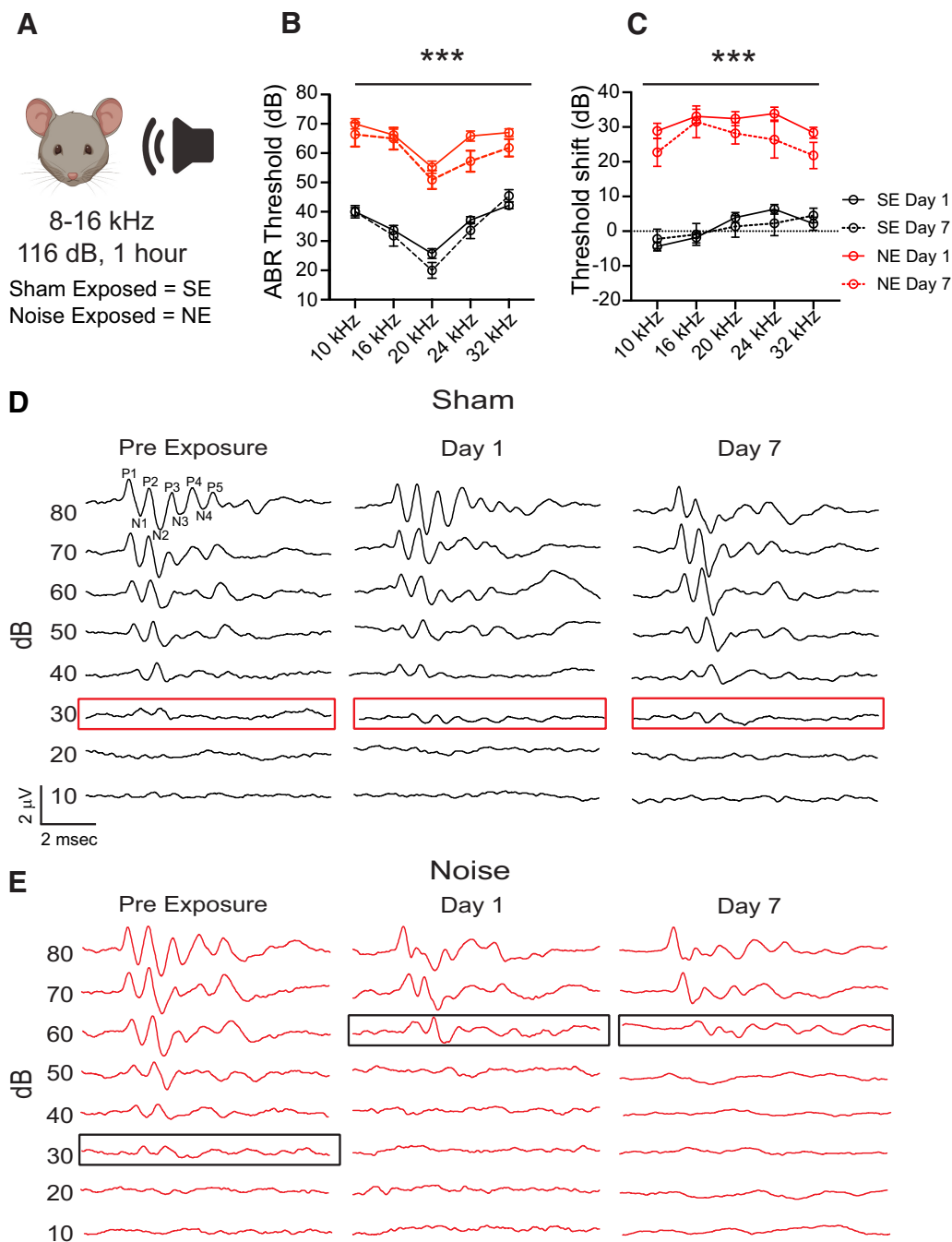
Figure 1. Mouse model of noise-induced peripheral damage. ***A***, Mice were unilaterally exposed to either an 8-16 kHz sound at 116 dB for 1 h or sham exposure. ***B***, ABR thresholds in NE and SE mice. ***C***, ABR threshold shifts in NE, but not SE, mice ***D***, ***E***, Representative ABR traces in response to a 16 kHz stimulus, collected before exposure, 1 d, and 7 d after exposure, illustrate threshold elevations in NE, but not SE, mice. ***A–E***, Day 1 SE: $n = 51$ mice; day 7 SE: $n = 18$ mice; day 1 NE: $n = 54$ mice; day 7 NE: $n = 17$ mice. Black represents SE. Red represents NE. Data are mean $\pm$ SEM. Table 1 lists detailed statistical values and tests. ***$p < 0.001$.

but not SE, mice displayed elevated ABR thresholds 1 d after NE, which remained elevated 7 d after NE (Fig. 1*B–E*). These results validate that this noise trauma protocol causes persistent noise-induced hearing loss (Table 1). We thus used this protocol to study mechanisms of cortical plasticity after peripheral damage.

No changes in the intrinsic excitability of either L2/3 PNs or somatostatin-expressing neurons (SOMs) after peripheral trauma

To investigate the effect of noise-induced peripheral damage on the plasticity of cortical neurons, we used whole-cell patch-clamp

recordings in acute brain slices containing AC, prepared at 1 and 7 d after NE or SE. Recordings were targeted to PNs in the right AC, contralateral to the noise-exposed ear. PNs were labeled red by an injection of retrogradely transported fluorescent microbeads (retrobeads) in the contralateral (left) AC (Fig. 2*A*,*B2*). These beads label a subtype of PNs that project to the contralateral cortex, called corticocallosal (Ccal) neurons. Because this approach can also label a small proportion of PVs (Rock et al., 2018), recordings were targeted to labeled neurons that were non–fast-spiking, and had larger cell bodies and distinct PN shape, thus ensuring recordings from L2/3 Ccal (PNs). In coronal brain
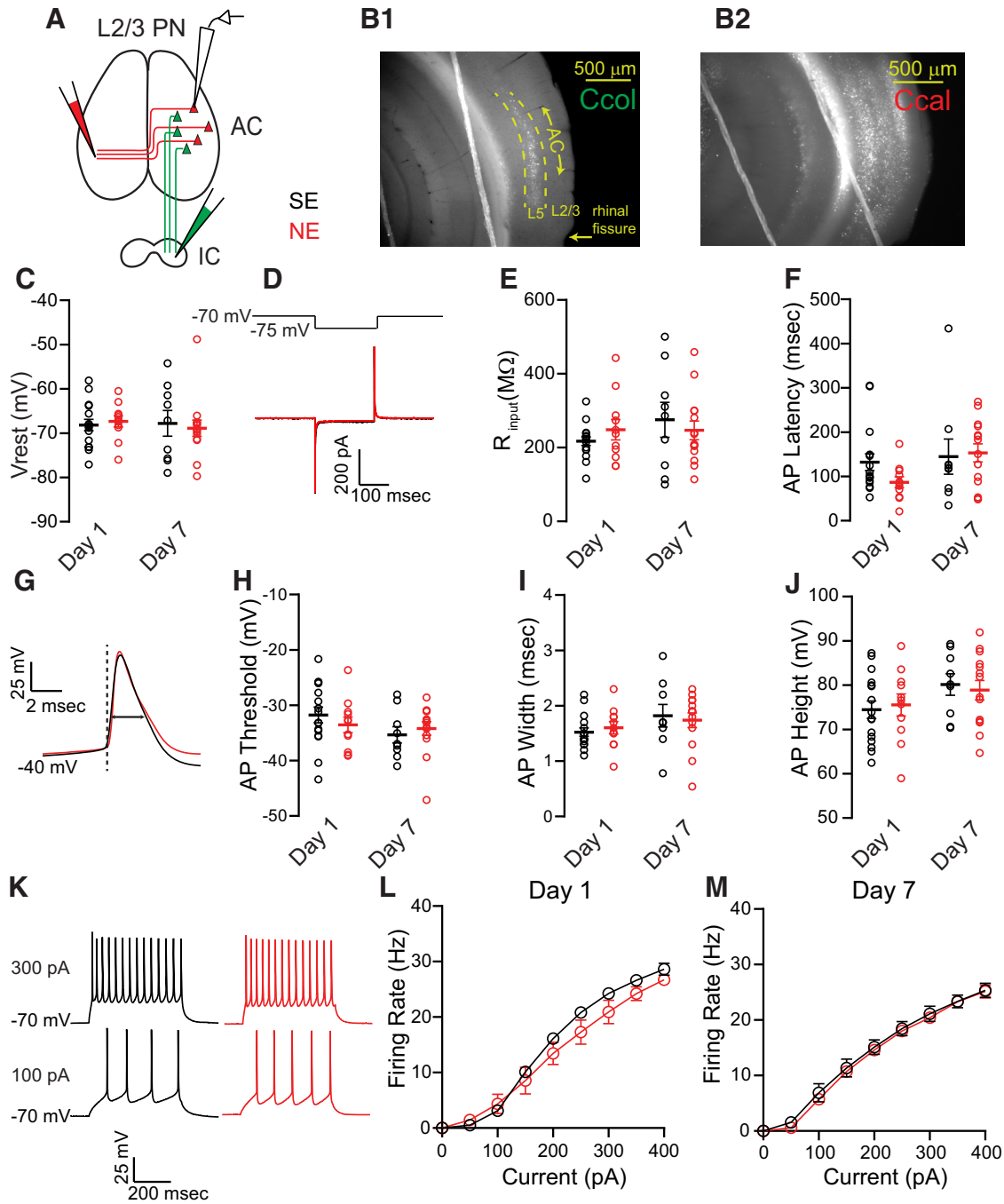
Figure 2. No changes in the intrinsic excitability of L2/3 PNs after NE. ***A***, Diagram of red retrobead injections to demarcate AC and label PNs. To localize AC in acute cortical slices, green retrobeads were injected into the right inferior colliculus. Red beads were injected into the left AC to label PNs in right AC. ***B1***, ***B2***, Low-magnification images (4×) showing green retrograde labeling of L5 corticocollicular neurons (Ccol) and red retrograde labeling of Ccal PNs. Recordings were targeted to red-labeled PNs at right AC. ***C–E***, Subthreshold intrinsic properties, including V_{rest} and R_{input}. ***D***, Hyperpolarizing pulse (from −70 to −75 mV, top) in voltage-clamp mode results in transient current responses (bottom). The difference between baseline and steady-state hyperpolarized current is used to calculate the input resistance. ***F–J***, Suprathreshold intrinsic properties, including AP latency, AP threshold, AP width, and AP height. ***G***, Example AP waveform. Dotted line indicates AP threshold. Arrow indicates AP width. ***K***, Representative firing of PN in response to 100 and 300 pA depolarizing current. ***L***, ***M***, Average firing frequency as a function of injected current for PNs (f-I curve). ***A–M***, Day 1 SE: $n = 16$ cells, 9 mice; day 1 NE: $n = 11$ cells, 8 mice; day 7 SE: $n = 9$ cells, 7 mice; day 7 NE: $n = 14$ cells, 6 mice. For all figures: each circle without an error bar represents one cell. Table 2 lists detailed statistical values and tests.

slices, AC is not easily localized, as there are no clear cytoarchitectural boundaries. To localize AC, we labeled L5 corticocollicular neurons, which project to the inferior colliculus, by injecting green retrobeads in the inferior colliculus (Fig. 2A). Consistent with previous studies (Joshi et al., 2015), we found robust bead labeling in L5 of the AC (Fig. 2B1). The dorsal-ventral boundaries of the L5 green bead labeling, in combination with anatomic

landmarks such as the rhinal fissure and hippocampus, were used to localize AC in our brain slice preparation. To evaluate the effect of peripheral damage on the intrinsic excitability of labeled L2/3 PNs, we performed our recordings in the presence of blockers of AMPA, NMDA, and GABA$_A$ receptor-mediated neurotransmission (see Materials and Methods). We found that subthreshold intrinsic properties, such as resting membrane

potential (V_{rest}), and R_{input} were not different between NE- and SE-exposed mice either at 1 or 7 d after exposure (Fig. 2C–E; Table 2). Suprathreshold intrinsic properties, such as AP latency, threshold, width, and height, were also not different (Fig. 2F–J; Table 2). Consistent with no change in either subthreshold or suprathreshold intrinsic excitability, we did not observe any significant changes in the firing frequency-current (f-I) curve at either 1 or 7 d after exposure (Fig. 2K–M; Table 2). Together, these results suggest that there are no changes in the intrinsic excitability of L2/3 PNs after peripheral damage at either 1 or 7 d after noise trauma.

We next investigated whether the intrinsic excitability of L2/3 SOMs was altered after noise trauma. SOMs represent a diverse class of interneurons with distinct morphologic and functional features. These neurons shape inhibition and excitation in cortex, for they have axons that extend across several cortical layers and target both PNs and PVs (Harris and Shepherd, 2015; Tremblay et al., 2016). To target L2/3 SOMs, we used SOM-GFP mice, in which SOMs are labeled green (Fig. 3B). AC was localized as described in Figure 2A. No significant effect of NE compared with SE was observed in either subthreshold (Fig. 3C–E; Table 2) or suprathreshold intrinsic properties (Fig. 3F–M; Table 2). Together, these results show no changes in the intrinsic excitability of L2/3 SOMs after peripheral damage at either 1 or 7 d after noise trauma.

Reduction in the intrinsic excitability of L2/3 PVs 1, but not 7, d after NE

Next, we investigated the effect of noise-induced peripheral damage on L2/3 PVs. In the neocortex, PVs are the most numerous inhibitory neuronal cell types and form synapses on critical sites for AP generation, such as the perisomatic region and axon initial segment of PNs and PVs (Tremblay et al., 2016). We crossed PV-Cre mice with Ai14 mice to label PVs with fluorescent TdTomato, and we localized AC via retrobead injection as described previously (Fig. 2A). Recordings were targeted to Td-Tomato-labeled L2/3 PVs in AC (Fig. 4A,B). We found that PV intrinsic excitability was significantly reduced 1, but not 7, d after NE compared with SE, as evidenced by a hyperpolarization of V_{rest} and a depolarization of the AP threshold (Fig. 4C–E; Table 2, $n = 20$ cells, 6 mice for SE, $n = 25$ cells, 9 mice for NE). We also observed an overall reduction in the firing frequency (f-I curves) of L2/3 PVs 1, but not 7, d after NE (Fig. 4G,H; Table 2, $n = 20$ cells, 6 mice for SE, $n = 25$ cells, 9 mice for NE). There were no significant differences in the other intrinsic excitability parameters, such as R_{input}, AP width, height, and latency (Fig. 4I–M; Table 2). Together, these results demonstrate a rapid, transient, cell type-specific decrease in the intrinsic excitability of L2/3 PVs 1 d after peripheral trauma.

Sustained delayed-rectifier and transient I_A potassium currents in L2/3 PVs are likely unchanged 1 d after NE

We next investigated the ion channel mechanisms that underlie the reduced PV intrinsic excitability. We investigated voltage-gated potassium channels, for these channels are very plastic, and their plasticity can powerfully modulate neuronal excitability in response to noise-induced hearing loss or even to nontraumatic changes in the acoustic environment (Song et al., 2005; Strumbos et al., 2010; Li et al., 2013, 2015; Gainey et al., 2018; Wu and Kaczmarek, 2021). Sustained delayed-rectifier potassium channels are good candidates to regulate PV excitability, as they are expressed in PV neurons and regulate the AP threshold in an activity-dependent manner (Goldberg et al., 2008; Dehorter

et al., 2015). Thus, we investigated whether changes in sustained delayed-rectifier potassium currents are involved. To isolate these currents, we blocked synaptic transmission as before, as well as calcium-activated potassium, KCNQ, sodium, and HCN channels (see Materials and Methods). We used a voltage-clamp protocol, where cells were held at -100 mV for 2.5 s to allow for recovery from inactivation. A series of depolarizing voltage steps (10 mV steps from -70 to -10 mV) were delivered for 300 ms to evoke the sustained delayed-rectifier potassium currents (Fig. 5A,B). We also delivered a series of hyperpolarizing voltage steps (from -100 to -80 mV, in 5 mV steps) to measure the linear leak current (Fig. 5C). Since leak currents are linear and not voltage-gated, the measured leak current was extrapolated to the series of depolarizing steps and then subtracted. Leak current was not different between SE and NE (Fig. 5D; Table 2). The depolarizing voltage steps activate the sustained delayed-rectifier currents and the rapidly inactivating A-type potassium currents (I_A) (Fig. 5B). Because I_A currents inactivate within the first ~50 ms of stimulus presentation, we measured the sustained delayed-rectifier currents 200-300 ms after the initiation of the depolarizing steps. We found no differences in the sustained delayed-rectifier potassium currents between SE and NE mice in L2/3 PVs (Fig. 5E; Table 2).

Next, we assessed the I_A currents. To isolate I_A, we used a combination of pharmacology and voltage-clamp protocols (Guan et al., 2011; Gainey et al., 2018). Namely, we used a potassium internal solution with 5 mM BAPTA, and a low Ca^{2+} bath solution to reduce calcium-activated potassium currents (see Materials and Methods). We also blocked synaptic transmission, as well as sodium channels and sustained delayed-rectifier potassium currents (see Materials and Methods). Cells were held at -100 mV for 2.5 s to allow for recovery after inactivation. On interleaved trials, we applied a depolarizing voltage step to 0 mV for 300 ms, which was preceded either by a 200 ms prepulse to -70 mV, where I_A is not inactivated, or by a 200 ms prepulse to -40 mV, where I_A is inactivated (Fig. 5F–H). Although most channels underlying the A-type current are not inactivated at -70 mV (Coetzee et al., 1999), Kv 4.2 channels may be partially inactivated at -70 mV (Ye et al., 2022). To isolate the rapidly inactivating I_A potassium currents, we subtracted the current evoked by the -40 mV sweep from the current evoked by the -70 mV sweep (Fig. 5G). We observed no differences in I_A currents in L2/3 PVs between NE and SE mice (Fig. 5H,I; Table 2). Together, although these results do not provide full accounting of the activation and inactivation functions of I_A, they suggest that neither sustained delayed-rectifier nor transient I_A potassium currents are likely involved in the decreased intrinsic excitability of L2/3 PVs 1 d after peripheral damage.

Upregulation of KCNQ channel activity in L2/3 PVs contributes to the decreased PV intrinsic excitability 1 d after NE

Kv7 (KCNQ) channels are expressed in PVs in the hippocampus and somatosensory cortex and are crucial for regulating their intrinsic excitability in these neurons (Soh et al., 2018). Furthermore, a recent study showed changes of KCNQ gene expression in AC PVs after long-term enhancement of NMDA receptor function (Xia et al., 2021). We therefore decided to investigate the role of KCNQ potassium channels in AC L2/3 excitability PVs 1 and 7 d after exposure. Namely, we interrogated whether changes in KCNQ channel activity contribute to the reduction in the intrinsic excitability of L2/3 PVs. If an increase in KCNQ activity contributes to the reduced firing rate (f-I curve) of PVs, a KCNQ channel opener would have a smaller effect on reducing the firing frequency of PVs in NE compared with SE mice.
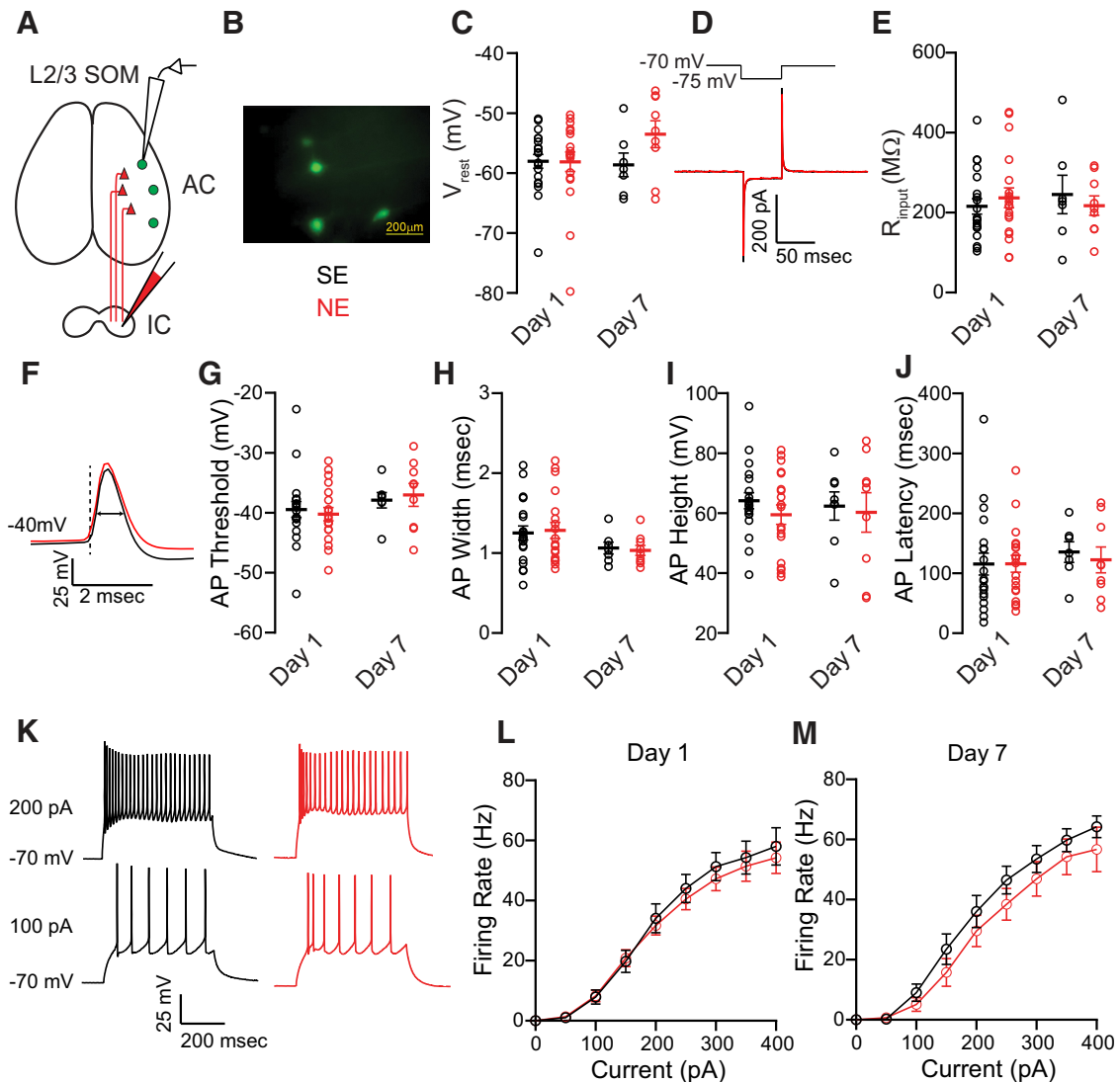
Figure 3. No changes in the intrinsic excitability of L2/3 SOMs after NE. ***A***, Diagram of red retrobead injection in the inferior colliculus to demarcate AC. ***B***, Example of GFP-labeled SOMs in SOM-GFP mouse brain slice; recordings were targeted to GFP-labeled L2/3 SOMs. ***C–E***, Subthreshold intrinsic properties. ***F–J***, Suprathreshold properties. ***K***, Representative firing of SOM in response to 100 and 200 pA depolarizing current. ***L, M***, Average f-I curve for SOMs. ***A–M***, Day 1 SE: $n = 20$ cells, 13 mice; day 1 NE: $n = 19$ cells, 9 mice; day 7 SE: $n = 7$ cells, 4 mice; day 7 NE: $n = 9$, cells 5 mice. Table 2 lists detailed statistical values and tests.

Moreover, we would expect no differences in the firing frequency in SE and NE mice after application of the opener because of this occluding effect. To answer this question, we delivered depolarizing current steps as in Figure 4F, G, and measured the firing frequency of PVs from NE and SE mice, before and after the application of the KCNQ channel opener retigabine, which enhances KCNQ currents by shifting the voltage dependence of the channel to more hyperpolarized potentials (Tatulian et al., 2001; Xiong et al., 2008). We found that retigabine caused an overall decrease in firing (Fig. 6A; Table 3, $n = 9$ cells, 6 mice for SE; $n = 9$ cells, 5 mice for NE). Given the interaction between drug and exposure, to further probe the effect of retigabine on NE versus SE mice, we analyzed the initial slope of the f-I curve (150-250 pA). When we compared the initial slope between SE- and NE-exposed mice, we found that retigabine reduced the slope in SE, but not NE, mice, and there were no differences in the slope of SE and NE mice (Fig. 6B; Table 3, $n = 9$ cells, 6 mice for SE; $n = 9$ cells, 5 mice for NE). These results are consistent with the notion that the effect of NE in reducing firing rates is due, at least in

part, to the modulation of KCNQ channels. Together, these results support that increases in KCNQ channel activity contribute to the decrease of intrinsic excitability of L2/3 PVs 1 d after noise trauma.

Since we observed decreased intrinsic excitability of L2/3 PVs 1 d after noise trauma, which recovers to baseline by 7 d, we asked whether this recovery of intrinsic excitability is also associated with an effect of retigabine in the slope of the f-I curve in both SE and NE mice 7 d after the exposure. Unlike what we found for 1 d after exposure, retigabine caused a decrease in the slope of the f-I curve in both SE and NE mice 7 d after the exposure (Fig. 6C,D; Table 3, $n = 6$ cells, 3 mice for SE; $n = 5$ cells, 3 mice for NE). Together, these results suggest an increase in KCNQ channel function in PVs at 1, but not 7, d after NE, which contributes to the enhanced intrinsic excitability of these neurons 1 d after NE.

To confirm our conclusions on the increased KCNQ channel plasticity 1 d after NE, we next directly measured KCNQ currents in AC L2/3 PVs. To do this, we performed whole-cell voltage-clamp experiments. To isolate the KCNQ currents, we blocked
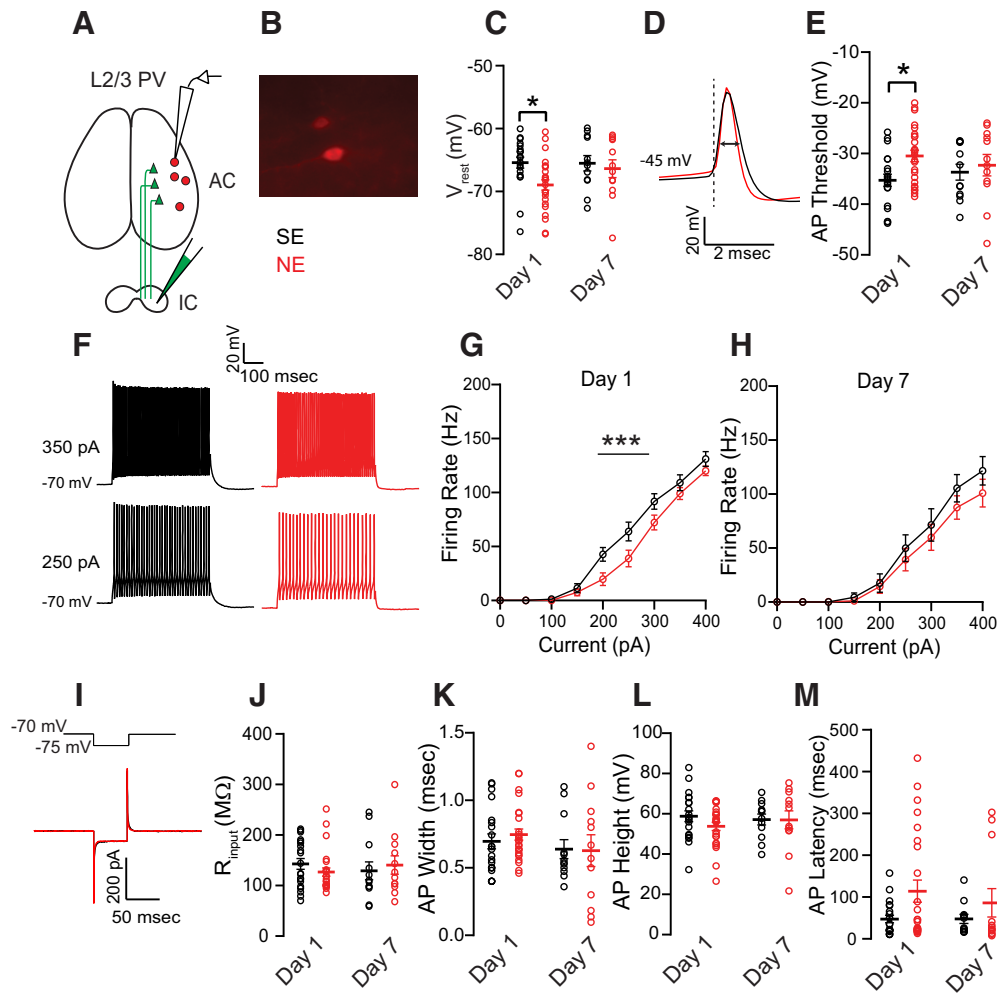
Figure 4. Reduction in the intrinsic excitability of L2/3 PVs 1, but not 7, d after NE. *A*, Diagram of retrobead injection in the inferior colliculus to demarcate AC. *B*, Example of TdTomato (red)-labeled PVs in PV-Cre X Ai14 mouse brain slice. Recordings were targeted to red-labeled L2/3 PVs. *C*, V_{rest}, is hyperpolarized 1, but not 7, d after NE. *D*, Example AP waveform. Dotted line indicates AP threshold. Arrow indicates AP width. *E*, AP threshold is depolarized 1, but not 7, d after exposure. *F*, Representative firing from SE (black) and NE (red) 1 d after exposure. *G*, *H*, Firing frequency is reduced at 1, but not 7, d after NE. *I–M*, No change in R_{input}, AP width, AP height, and AP latency. *A–M*, Day 1 SE: $n = 20$ cells, 6 mice; day 1 NE: $n = 25$ cells, 9 mice; day 7 SE: $n = 12$ cells, 7 mice; day 7 NE: $n = 12$ cells, 6 mice. Table 2 lists detailed statistical values and tests. ****p < 0.001*. **p < 0.05*.

synaptic transmission, as well as HCN and calcium channels (see Materials and Methods). We held PVs at −30 mV for 5 s to activate KCNQ channels, and then stepped the voltage to −50 mV to reveal the characteristic slowly deactivating KCNQ current (Fig. 7A). To further isolate the KCNQ current, the KCNQ channel blocker XE-991 (10 μM) was applied, and the remaining current was then subtracted from the control current to reveal the XE-991-sensitive current, the KCNQ current (Fig. 7A, green). When we compared KCNQ currents between NE and SE mice, we found a significant increase in the KCNQ current in L2/3 PVs 1 d after NE (Fig. 7C, $p = 0.02$, Mann–Whitney test, $n = 7$ cells, 5 mice for SE; $n = 6$ cells, 5 mice for NE). This result further supports our conclusion on increased KCNQ channel activity 1 d after NE in AC L2/3 PV neurons.

To probe for potential changes in the voltage-dependent gating of KCNQ channels, we conducted voltage ramp experiments. When we delivered slow voltage ramps (10 mV/s; −70 to −10 mV), we revealed an outward current that was partially blocked by XE-991 (Fig. 7D). The remaining current after XE-991 application was subtracted from the control current to isolate the XE-991-sensitive, KCNQ current (Fig. 7D). To correct for the voltage drop because of the residual R_{series} (after 60%-80% R_{series} compensation),

we subtracted the voltage error (membrane current multiplied by the residual R_{series}) from the command voltage (Vm = Vcmd − (Im × residual R_{series})). We then interpolated to a common voltage curve and subtracted the XE-991-sensitive curve from the control current to create a common current–voltage curve between experimental conditions (Fig. 7E; see Materials and Methods). Despite these corrections, the voltage drop was too large to allow for the fitting of a Boltzmann function. Since fitting the data with a Boltzmann function was not appropriate, we did not measure either half-maximum activation voltage ($V_{1/2}$) or maximal conductance (G_{max}). Instead, we measured the minimal (threshold) activation voltage. Namely, we measured at what voltage the current increased >4 SDs from the mean baseline current and was maintained elevated for the rest of the ramp (Fig. 7E). After this analysis, we found that NE caused a hyperpolarization of the threshold activation voltage (Fig. 7F, $p = 0.024$, unpaired t test, $n = 4$ cells, 4 mice for SE; $n = 5$ cells, 5 mice for NE), consistent with increased KCNQ channel activity in noise-exposed mice.

Together, the increased KCNQ current (Fig. 7C), the more hyperpolarized threshold activation voltage of KCNQ channels (Fig. 7F), and the reduced effect of retigabine on the firing rate of PVs 1 d after NE (Fig. 6A,B) strongly suggest an increase in
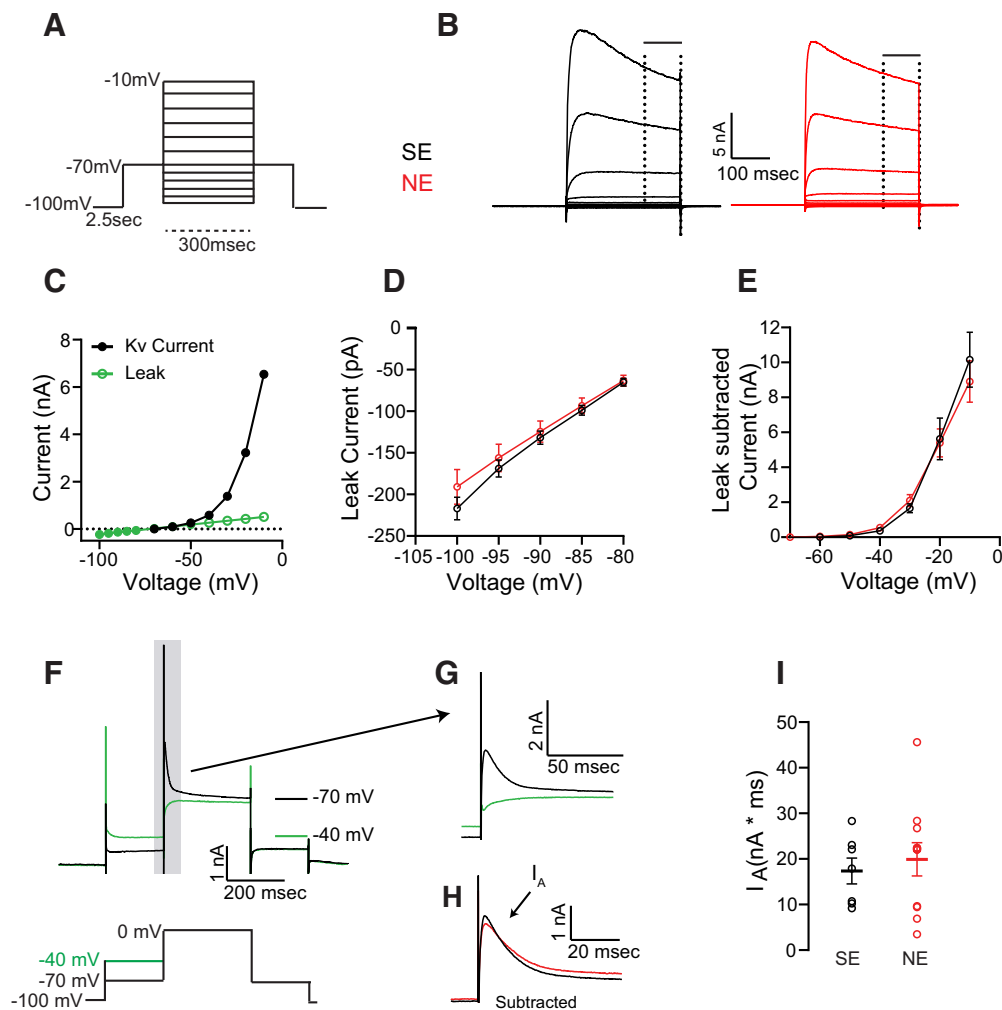
Figure 5. Sustained delayed-rectifier and transient I_A potassium currents in L2/3 PVs are unchanged 1 d after NE. ***A***, Voltage-clamp protocol for sustained delayed-rectifier current recordings. ***B***, Example current traces in response to voltage steps in ***A***. Steady-state current was measured as the mean current amplitude during the last 100 ms (solid line) of the 300 ms depolarizing pulse. ***C***, Example of measured leak current (green filled circles) and the extrapolated leak current (green open circles), which were subtracted from the steady-state current (black). ***D***, Leak currents were not different between NE and SE. ***E***, Leak subtracted currents were not different between NE and SE. ***F***, Voltage protocol (below) for recording I_A current recordings (top). ***G***, Traces from an example cell, showing currents elicited at 0 mV from the −70 mV (black) and the −40 mV prepulse (green). ***H***, I_A current, after subtracting the black from green trace for both SE (black) and NE (red). ***I***, Summary graph of I_A for SE and NE. ***A–E***, $n = 9$ cells, 5 mice for SE; $n = 12$ cells, 11 mice for NE. ***F–I***, $n = 7$ cells, 4 mice for SE; $n = 11$ cells, 6 mice for NE. Detailed statistical values and tests in Table 2. The format for the bottom part of this figure was inspired by Gainey et al. (2018, their Fig. 7).

KCNQ channel function 1 d after exposure, which contributes in the decreased intrinsic excitability of AC L2/3 PVs 1 d after NE (Fig. 4).

Discussion

Our results reveal a cell type-specific reduction in the intrinsic excitability of PVs in L2/3 AC 1 d after noise trauma. This is a transient reduction, for PV excitability returns to control (sham) levels by 7 d after noise trauma. Importantly, our results support an association between changes in KCNQ potassium channel activity and this reduction. Namely, we observed an increase in KCNQ channel activity, as evidenced by increased KCNQ currents and a hyperpolarization in the minimal activation voltage of KCNQ channels. This increased KCNQ channel activity contributes to the decreased excitability of L2/3 PVs 1, but not 7, d after acoustic trauma. Understanding the precise cellular and molecular mechanisms underlying cortical plasticity after peripheral injury is crucial for our knowledge of homeostatic plasticity mechanisms and may also inform future drug development efforts for the treatment of disorders that are associated with

maladaptive cortical plasticity triggered by peripheral trauma, such as tinnitus and hyperacusis.

The role and mechanisms of decreased PV intrinsic excitability in the plasticity of sensory cortex after peripheral injury

The canonical pathway for cortical plasticity after peripheral damage, or sensory deprivation, involves a rapid reduction in cortical GABAergic inhibition associated with the disinhibition of PNs soon after the insult, and a subsequent recovery of excitatory responses that occur on the timescale of 1 or more weeks (Gainey and Feldman, 2017). Recent evidence from the AC supports that a steep drop in PV-mediated inhibition to PNs is a predictor of auditory cortical response normalization after peripheral damage (Kuhlman et al., 2013; Resnik and Polley, 2017). Consistent with these findings on the important role of PV plasticity after peripheral trauma, our results reveal a rapid reduction in the intrinsic excitability of L2/3 PVs in AC 1 d after noise trauma. Importantly, our results on the KCNQ-related mechanism provide a novel biophysical mechanism for the reduction of PV intrinsic excitability after peripheral trauma.

PVs are well positioned to contribute significantly to rapid changes in excitatory activity after sensory organ injury. PVs, unlike VIPs or SOMs, receive direct thalamic input (Harris and Shepherd, 2015), and thus can sense and respond quickly to reductions of sensory input after peripheral trauma. Moreover, PVs efficiently regulate PN excitability as they form synapses on the perisomatic region and axon initial segment of PNs (Goldberg et al., 2008; Tremblay et al., 2016), which are critical sites of AP generation. As such, PVs have emerged as canonical regulators of plasticity in cortex across multiple sensory cortices; however, the precise underlying mechanisms of PV plasticity are less understood.

In the somatosensory cortex, whisker plucking induces a rapid and marked reduction of PV intrinsic excitability 1 d after trauma. This effect is associated with the upregulation of sustained delayed-rectifier potassium currents, likely mediated by Kv1 channels, and the rapidly inactivating I_A current, likely mediated by Kv1.4 and Kv4 channels (Gutman et al., 2005; Goldberg et al., 2008; Sun, 2009; Dehorter et al., 2015; Gainey et al., 2018). In the AC, we also found a reduction in intrinsic excitability of PVs. However, this reduction is associated with enhanced KCNQ potassium channel opening. These results suggest that, although the reduction of PV intrinsic excitability may be a common feature of plasticity across sensory cortices, the underlying ion channel mechanisms differ between cortices, perhaps to better serve the cellular and processing needs of each cortical area.

How does the reduced intrinsic excitability of PVs contribute to the AC network activity? One hypothesis is that reduced PV excitability can lead to an overall decrease in inhibition and thus to an enhancement of excitation which, in turn, may contribute to the recovery of PN sensory-evoked responses. However, there are two different models that can describe the network effects of inhibition in the AC: the inhibition stabilized network (ISN) (Kato et al., 2017), which is based on the strength of recurrent inhibition, and the cascaded feedforward model (CFF) (Moore et al., 2018), which is based on the multiple stages of cortical feedforward inhibition. Although the two models are not mutually exclusive, they can lead to different predictions on the effects of reduced excitability in PVs. According to the ISN model, a decrease in the intrinsic PV excitability might lead to enhanced PV activity in the network, along with enhanced PN activity. Based on the CFF model, a decrease in the intrinsic PV excitability might lead to layer- and/or site-specific changes in the activity of PVs. In a recent study, the activity of AC PNs and PVs was monitored before and after cochlear neural degeneration (Resnik and Polley, 2021). This degeneration was induced by bilateral cochlear round window application of ouabain, a Na^+-K^+ ATP-ase inhibitor, which electively eliminates Type I spiral ganglion neurons, which transmit virtually all afferent signals from cochlear inner hair cells to brainstem. Sound-evoked L2/3 PN responses were reduced soon after the trauma but recovered within a few days. Sound-evoked L2/3 PV responses were also reduced soon after the trauma but showed much less recovery, perhaps consistent with the CFF model. However,
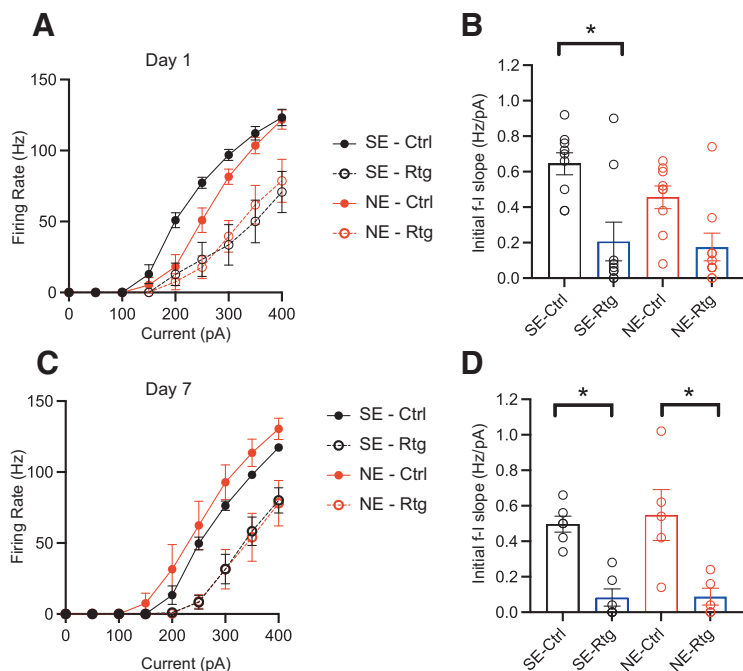
Figure 6. Upregulation of KCNQ channel activity in L2/3 PVs contributes to the decreased PV intrinsic excitability 1 d after NE. **A**, L2/3 PV f-I curves 1 d after SE or NE in control (Ctrl) or in retigabine (Rtg). **B**, f-I initial slope (150-250 pA). **A**, **B**, SE: $n = 9$ cells, 6 mice; NE: $n = 9$ cells, 5 mice. **C**, L2/3 PV f-I curves 7 d after SE or NE. **D**, f-I initial slope (150-250 pA). **C**, **D**, SE: $n = 6$ cells, 3 mice; NE: $n = 5$ cells, 3 mice. Table 3 lists detailed statistical values and tests. *$p < 0.05$.

spontaneous activity was enhanced in both cell types, at least soon after the trauma, perhaps consistent with the ISN model at these time points. These results suggest that, at different time points after peripheral trauma, the AC might be shifting from an ISN to a CFF operating regimen. Thus, while our results demonstrate an acute reduction in intrinsic excitability of PVs but not PNs or SOMs, the effect of this change on network activity might depend on the cortical operating regime (ISN or CFF) at different time points after the noise trauma. Moreover, noise trauma affects different neural and sensory cells on the cochlea compared with ouabain application, and thus might affect central plasticity differentially. To better understand the network effects of our finding, our future studies will include monitoring of the sound-evoked and spontaneous activity of PNs and interneurons at different AC cortical sites and time points after noise trauma.

Comparison of adult cortical plasticity after peripheral sensory damage with critical period developmental plasticity
Adult cortical plasticity and critical period developmental plasticity are thought to share common mechanisms, such as an initial reduction in GABAergic inhibition (Hensch, 2004; Cisneros-Franco and de Villers-Sidani, 2019; Persic et al., 2020). In this context, our results highlight an inhibitory plasticity mechanism that is consistent with mechanisms of developmental plasticity (Takesian and Hensch, 2013; Takesian et al., 2018; Persic et al., 2020), and thus support the notion that a decrease in PV intrinsic excitability may initiate a critical period-like state that allows for adult plasticity and perceptual recovery.

How could this decrease in PV intrinsic excitability initiate adult plasticity? Apart from the direct effects of reduced PV intrinsic excitability on network properties that were discussed earlier, a transient reduction in PV activity may gate adult plasticity through several additional mechanisms. One
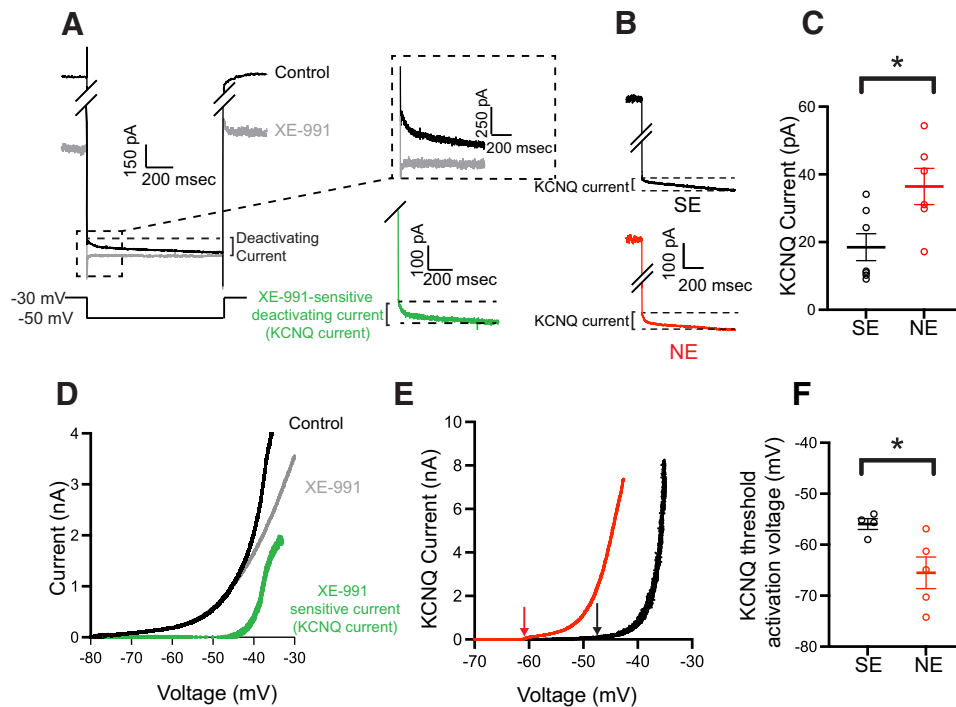
Figure 7. Increased KCNQ currents in L2/3 PVs 1 d after NE. **A**, Current elicited by 1 s hyperpolarization to −50 mV from a holding potential of −30 mV (bottom). Green trace represents the XE-991-sensitive KCNQ current. **B**, Representative SE and NE KCNQ current traces. **C**, KCNQ current is increased in NE compared with SE ($p = 0.02$, Mann–Whitney test, $n = 7$ cells, 5 mice for SE; $n = 6$ cells, 5 mice for NE). **D**, Slow voltage ramps (10 mV/s) reveal an outward current trace (black) that is partially blocked by XE-991 (gray current trace). Subtraction of the gray trace from the black trace reveals the XE-991-sensitive KCNQ current (green). **E**, Example current–voltage curve of XE-991-sensitive current. Black represents SE. Red represents NE. Arrow indicates the minimal (threshold) voltage activation threshold. **F**, The threshold voltage activation is more hyperpolarized in NE, compared with SE cells ($p = 0.024$, unpaired t test; $n = 4$ cells, 4 mice for SE; $n = 5$ cells, 5 mice for NE). *$p < 0.05$.

such mechanism includes changes in spike timing-dependent plasticity and LTP at excitatory synapses. For example, decreased inhibition via application of GABAR antagonists increases LTP at excitatory synapses (Kirkwood and Bear, 1994; Harauzov et al., 2010). Peripheral injury-induced reductions in PV excitability may also trigger molecular pathways that promote structural changes that may, in turn, permit enhanced excitatory synaptic strength (Mataga et al., 2004). Moreover, a reduction in PV excitability may lead to more synchronous network activity and coherence (Doischer et al., 2008). Future experiments are needed to determine if and how these mechanisms might be involved in adult cortical plasticity after peripheral injury.

Timing and different forms of intrinsic plasticity after peripheral damage

Our findings complement and extend previous findings on the time course of plasticity after acoustic trauma. Namely, previous studies highlight an increase in PN intrinsic excitability 10 d after noise exposure (Yang et al., 2012). Although our studies differ in species, exposure intensity, and timing after NE, these studies and our results might also suggest that PN intrinsic excitability may increase at later time points after the peripheral trauma, for we only investigated neuronal excitability up to 7 d after noise trauma. This hypothesis, albeit not tested here, would be consistent with previous studies in the somatosensory system suggesting that PV intrinsic plasticity occurs first and permits the subsequent homeostatic modulation of PNs, marked by increases in PN intrinsic excitability and excitatory synaptic scaling (Gainey and Feldman, 2017).

Moreover, our results complement and extend previous mechanisms of intrinsic plasticity, such as a hearing loss-induced

reduction in inhibitory synaptic strength in the inferior colliculus because of decreased function of potassium-dependent chloride transporter function (Vale et al., 2003). Although the animals were younger in that study, both studies provide evidence for intrinsic plasticity of inhibitory neurons after hearing loss.

The role of KCNQ channels in cortical plasticity and hyperexcitability-related disorders

KCNQ channels have been described as the molecular "brakes" of neuronal excitability (Delmas and Brown, 2005; Vigil et al., 2020). Mutations and/or activity-dependent dysfunction of these channels lead to disorders, such as epilepsy, tinnitus, neuropathic pain, traumatic brain injury, and developmental and mood disorders (Biervert et al., 1998; Soldovieri et al., 2011; Li et al., 2013; Oyrer et al., 2018; Allen et al., 2020; Vigil et al., 2020). In response to similar noise trauma, KCNQ activity is reduced in the PNs (fusiform cells) of the dorsal cochlear nucleus, an auditory brainstem nucleus (Li et al., 2013, 2015). In fusiform cells, KCNQ channel activity was reduced uniformly 4 d after noise trauma. Seven days after noise trauma, mice with persistent reductions in KCNQ currents developed dorsal cochlear nucleus hyperexcitability and tinnitus, whereas mice that showed a recovery of KCNQ channel activity did not develop tinnitus (Li et al., 2013, 2015). These data suggest that, although a transient KCNQ modulation is a common and powerful mechanism to regulate intrinsic excitability in response to changes in peripheral input, prolonged modulation leads to hyperexcitability and hyperexcitability-related disorders. Consistent with this, persistent modulation of cortical KCNQ channel activity via deletion of KCNQ2/3 channels from PVs throughout development also leads to excitatory network hyperexcitability *in vivo*,

Table 1. Statistical values for Figure 1

Figure	Statistical test	Effect of exposure	Effect of time	Effect of frequency	Effect of frequency × exposure × time
1B	Three-way ANOVA	$p < 0.0001$	$p = 0.0100$	$p < 0.0001$	$p = 0.6576$
1C	Three-way ANOVA	$p < 0.0001$	$p = 0.2180$	$p = 0.0080$	$p = 0.5080$
	10 kHz	16 kHz	20 kHz	24 kHz	32 kHz
1B, D1 SE vs D1 NE	$p < 0.0001$	$p < 0.0001$	$p < 0.0001$	$p < 0.0001$	$p < 0.0001$
1B, D7 SE vs D7 NE	$p < 0.0001$	$p < 0.0001$	$p < 0.0001$	$p = 0.0002$	$p = 0.0770$
1B, D1 SE vs D7 SE	$p > 0.9999$	$p > 0.9999$	$p = 0.9935$	$p > 0.9999$	$p > 0.9999$
1B, D1 NE vs D7 NE	$p > 0.9999$	$p > 0.9999$	$p > 0.9999$	$p = 0.7291$	$p = 0.9977$
1C, D1 SE vs D1 NE	$p < 0.0001$	$p < 0.0001$	$p < 0.0001$	$p < 0.0001$	$p < 0.0001$
1C, D7 SE vs D7 NE	$p = 0.0090$	$p = 0.0020$	$p = 0.0010$	$p = 0.0080$	$p = 0.0050$
1C, D1 SE vs D7 SE	$p > 0.9999$	$p > 0.9999$	$p > 0.9999$	$p > 0.9999$	$p > 0.9999$
1C, D1 NE vs D7 NE	$p = 0.9960$	$p > 0.9999$	$p > 0.9999$	$p = 0.9940$	$p = 0.9700$

Table 2. Statistical values for Figures 2–5

Figure	Statistical test	Effect of exposure	Effect of time	Interaction effect	Day 1 SE vs NE	Day 7 SE vs NE
2C, V_{rest}	Two-way ANOVA, Bonferroni	$p = 0.941$	$p = 0.752$	$p = 0.623$	$p > 0.999$	$p > 0.999$
2E, R_{input}	Two-way ANOVA, Bonferroni	$p = 0.961$	$p = 0.300$	$p = 0.273$	$p = 0.792$	$p = 0.952$
2F, AP latency	Two-way ANOVA, Bonferroni	$p = 0.426$	$p = 0.095$	$p = 0.251$	$p = 0.305$	$p > 0.999$
2H, AP threshold	Two-way ANOVA, Bonferroni	$p = 0.829$	$p = 0.144$	$p = 0.313$	$p = 0.728$	$p > 0.999$
2I, AP width	Two-way ANOVA, Bonferroni	$p = 0.989$	$p = 0.096$	$p = 0.534$	$p > 0.999$	$p > 0.999$
2J, AP height	Two-way ANOVA, Bonferroni	$p = 0.965$	$p = 0.600$	$p = 0.617$	$p > 0.999$	$p > 0.999$
2L, D1 f-I curve	Two-way ANOVA	$p = 0.291$				
2M, D7 f-I curve	Two-way ANOVA	$p = 0.619$				
3C, V_{rest}	Two-way ANOVA, Bonferroni	$p = 0.177$	$p = 0.282$	$p = 0.164$	$p > 0.999$	$p = 0.210$
3E, R_{input}	Two-way ANOVA, Bonferroni	$p = 0.910$	$p = 0.910$	$p = 0.403$	$p = 0.40$	$p > 0.999$
3G, AP threshold	Two-way ANOVA, Bonferroni	$p = 0.978$	$p = 0.136$	$p = 0.600$	$p > 0.999$	$p > 0.999$
3H, AP width	Two-way ANOVA, Bonferroni	$p = 0.981$	$p = 0.056$	$p = 0.782$	$p > 0.999$	$p > 0.999$
3I, AP height	Two-way ANOVA, Bonferroni	$p = 0.422$	$p = 0.902$	$p = 0.762$	$p > 0.999$	$p > 0.999$
3J, AP latency	Two-way ANOVA, Bonferroni	$p = 0.758$	$p = 0.758$	$p = 0.744$	$p = 0.69$	$p > 0.999$
3L, D1 f-I curve	Two-way ANOVA	$p = 0.619$				
3M, D7 f-I curve	Two-way ANOVA	$p = 0.306$				
4C, V_{rest}	Two-way ANOVA, Bonferroni	$p = 0.014$	$p = 0.232$	$p = 0.214$	$p = 0.044$	$p > 0.999$
4E, AP threshold	Two-way ANOVA, Bonferroni	$p = 0.040$	$p = 0.939$	$p = 0.253$	$p = 0.016$	$p > 0.999$
4G, D1 f-I curve	Two-way ANOVA	$p < 0.001$				
4H, D7 f-I curve	Two-way ANOVA	$p = 0.074$				
4J, R_{input}	Two-way ANOVA, Bonferroni	$p = 0.860$	$p = 0.996$	$p = 0.256$	$p = 0.59$	$p = 0.944$
4K, AP width	Two-way ANOVA, Bonferroni	$p = 0.780$	$p = 0.195$	$p = 0.652$	$p > 0.999$	$p > 0.999$
4L, AP height	Two-way ANOVA, Bonferroni	$p = 0.374$	$p = 0.788$	$p = 0.407$	$p = 0.30$	$p > 0.999$
4M, AP latency	Two-way ANOVA, log transformed data, Bonferroni	$p = 0.323$	$p = 0.538$	$p = 0.354$	$p = 0.216$	$p > 0.999$
5D, Leak current	Two-way ANOVA	$p = 0.190$		$p = 0.270$		
5E, L-subtracted current	Two-way ANOVA	$p = 0.091$		$p = 0.357$		
5I, I_A current	Unpaired t test	$p = 0.590$				

Table 3. Statistical values for Figure 6

Figure	Statistical test	Effect of current	Effect of exposure	Effect of drug	Effect of current × exposure × drug
6A	Three-way ANOVA	$p < 0.0001$	$p = 0.0030$	$p < 0.0001$	$p = 0.619$
6C	Three-way ANOVA	$p < 0.0001$	$p = 0.0769$	$p < 0.0001$	$p = 0.952$

Figure	Statistical test	Main effect	SE-Ctrl vs SE-Rtg	NE-Ctrl vs NE-Rtg	SE-Ctrl vs NE-Ctrl	SE-Rtg vs NE-Rtg
6B	Friedman's test	$p = 0.003$	$p = 0.028$	$p = 0.252$	$p = 0.396$	$p = 0.917$
6D	Friedman's test	$p = 0.004$	$p = 0.005$	$p = 0.004$	$p = 0.998$	$p > 0.999$

likely through remodeling of cortical excitation and inhibition (Soh et al., 2018). Here, we report a rapid and brief upregulation of KCNQ currents in L2/3 PVs after peripheral damage, suggesting that this modulation is adaptive and contributes to cortical recovery after injury. However, we did not test our mice for either tinnitus or hyperacusis, which can be the result of maladaptive plasticity.

KCNQ channels have been a successful target for drug development (Davoren et al., 2015; Manville and Abbott, 2018; Miceli et al., 2018; Seefeld et al., 2018; Ostacolo et al., 2020; Borgini et al., 2021). Retigabine, originally an FDA-approved KCNQ channel activator, was very effective in treating individuals with epilepsy (Tatulian et al., 2001; Gunthorpe et al., 2012). However, retigabine was removed from the market in 2017 because of

adverse side effects (Eskioglou et al., 2017). Since retigabine is no longer a viable treatment option, there is a great need for the development of safe and nontoxic KNCQ channel openers. To fill this unmet need, more potent, more specific, and less toxic KCNQ channel activators are currently being developed (Kumar et al., 2016; Liu et al., 2019; Zhang et al., 2019; French et al., 2022; Hernandez et al., 2022). In this context, our results reveal a time-, and cell type-specific therapeutic target that may advance the development of precision-medicine-based treatments in hearing loss and associated disorders (Tzounopoulos et al., 2019).

References

Allen NM, Weckhuysen S, Gorman K, King MD, Lerche H (2020) Genetic potassium channel-associated epilepsies: clinical review of the Kv family. Eur J Paediatr Neurol 24:105–116.

Auerbach BD, Rodrigues PV, Salvi RJ (2014) Central gain control in tinnitus and hyperacusis. Front Neurol 5:206.

Biervert C, Schroeder BC, Kubisch C, Berkovic SF, Propping P, Jentsch TJ, Steinlein OK (1998) A potassium channel mutation in neonatal human epilepsy. Science 279:403–406.

Borgini M, Mondal P, Liu R, Wipf P (2021) Chemical modulation of Kv7 potassium channels. RSC Med Chem 12:483–537.

Cederholm JM, Froud KE, Wong AC, Ko M, Ryan AF, Housley GD (2012) Differential actions of isoflurane and ketamine-based anaesthetics on cochlear function in the mouse. Hear Res 292:71–79.

Chambers AR, Resnik J, Yuan Y, Whitton JP, Edge AS, Liberman MC, Polley DB (2016) Central gain restores auditory processing following near-complete cochlear denervation. Neuron 89:867–879.

Cisneros-Franco JM, de Villers-Sidani É (2019) Reactivation of critical period plasticity in adult auditory cortex through chemogenetic silencing of parvalbumin-positive interneurons. Proc Natl Acad Sci USA 116:26329–26331.

Coetzee WA, Amarillo Y, Chiu J, Chow A, Lau D, McCormack T, Moreno H, Nadal MS, Ozaita A, Pountney D, Saganich M, Vega-Saenz de Miera E, Rudy B (1999) Molecular diversity of K^+ channels. Ann NY Acad Sci 868:233–285.

Davoren JE, et al. (2015) Discovery of a novel Kv7 channel opener as a treatment for epilepsy. Bioorg Med Chem Lett 25:4941–4944.

Dehorter N, Ciceri G, Bartolini G, Lim L, del Pino I, Marín O (2015) Tuning of fast-spiking interneuron properties by an activity-dependent transcriptional switch. Science 349:1216–1220.

Delmas P, Brown DA (2005) Pathways modulating neural KCNQ/M (Kv7) potassium channels. Nat Rev Neurosci 6:850–862.

Doischer D, Hosp JA, Yanagawa Y, Obata K, Jonas P, Vida I, Bartos M (2008) Postnatal differentiation of basket cells from slow to fast signaling devices. J Neurosci 28:12956–12968.

Eskioglou E, Perrenoud MP, Ryvlin P, Novy J (2017) Novel treatment and new drugs in epilepsy treatment. Curr Pharm Des 23:6389–6398.

French J, Porter R, Perucca E, Brodie M, Rogawski M, Pimstone S, Aycardi E, Harden C, Xu Y, Luzon C (2022) Phase 2b efficacy and safety of XEN1101, a novel potassium channel opener, in adults with focal epilepsy (X-TOLE)(P12-8.006). Seattle, WA: AAN Enterprises.

Froemke RC, Jones BJ (2011) Development of auditory cortical synaptic receptive fields. Neurosci Biobehav Rev 35:2105–2113.

Gainey MA, Aman JW, Feldman DE (2018) Rapid disinhibition by adjustment of PV intrinsic excitability during whisker map plasticity in mouse S1. J Neurosci 38:4749–4761.

Gainey MA, Feldman DE (2017) Multiple shared mechanisms for homeostatic plasticity in rodent somatosensory and visual cortex. Philos Trans R Soc Lond B Biol Sci 372:20160157.

Gilbert CD, Wiesel TN (1992) Receptive field dynamics in adult primary visual cortex. Nature 356:150–152.

Goldberg EM, Clark BD, Zagha E, Nahmani M, Erisir A, Rudy B (2008) K^+ channels at the axon initial segment dampen near-threshold excitability of neocortical fast-spiking GABAergic interneurons. Neuron 58:387–400.

Guan D, Horton LR, Armstrong WE, Foehring RC (2011) Postnatal development of A-type and Kv1- and Kv2-mediated potassium channel currents in neocortical pyramidal neurons. J Neurophysiol 105:2976–2988.

Gunthorpe MJ, Large CH, Sankar R (2012) The mechanism of action of retigabine (ezogabine), a first-in-class K^+ channel opener for the treatment of epilepsy. Epilepsia 53:412–424.

Gutman GA, Chandy KG, Grissmer S, Lazdunski M, McKinnon D, Pardo LA, Robertson GA, Rudy B, Sanguinetti MC, Stühmer W, Wang X (2005) International Union of Pharmacology: LIII. Nomenclature and molecular relationships of voltage-gated potassium channels. Pharmacol Rev 57:473–508.

Harauzov A, Spolidoro M, DiCristo G, De Pasquale R, Cancedda L, Pizzorusso T, Viegi A, Berardi N, Maffei L (2010) Reducing intracortical inhibition in the adult visual cortex promotes ocular dominance plasticity. J Neurosci 30:361–371.

Harris KD, Shepherd GM (2015) The neocortical circuit: themes and variations. Nat Neurosci 18:170–181.

Hensch TK (2004) Critical period regulation. Annu Rev Neurosci 27:549–579.

Henton A, Tzounopoulos T (2021) What's the buzz? The neuroscience and the treatment of tinnitus. Physiol Rev 101:1609–1632.

Hernandez CC, Tarfa RA, Miguel IL, Liu R, Mondal P, Hill C, Duncan RK, Tzounopoulos T, Stephenson CRJ, O'Meara MJ, Wipf P (2022) Development of an automated screen for Kv7.2 potassium channels and discovery of a new agonist chemotype. Bioorg Med Chem Lett 71:128841.

Joshi A, Middleton JW, Anderson CT, Borges K, Suter BA, Shepherd GM, Tzounopoulos T (2015) Cell-specific activity-dependent fractionation of layer 2/3→5B excitatory signaling in mouse auditory cortex. J Neurosci 35:3112–3123.

Kaas JH, Krubitzer LA, Chino YM, Langston AL, Polley EH, Blair N (1990) Reorganization of retinotopic cortical maps in adult mammals after lesions of the retina. Science 248:229–231.

Kato HK, Asinof SK, Isaacson JS (2017) Network-level control of frequency tuning in auditory cortex. Neuron 95:412–423.e4.

Kinnischtzke AK, Sewall AM, Berkepile JM, Fanselow EE (2012) Postnatal maturation of somatostatin-expressing inhibitory cells in the somatosensory cortex of GIN mice. Front Neural Circuits 6:33.

Kirkwood A, Bear MF (1994) Hebbian synapses in visual cortex. J Neurosci 14:1634–1645.

Kotak VC, Fujisawa S, Lee FA, Karthikeyan O, Aoki C, Sanes DH (2005) Hearing loss raises excitability in the auditory cortex. J Neurosci 25:3908–3918.

Kuhlman SJ, Olivas ND, Tring E, Ikrar T, Xu X, Trachtenberg JT (2013) A disinhibitory microcircuit initiates critical-period plasticity in the visual cortex. Nature 501:543–546.

Kumar M, Reed N, Liu R, Aizenman E, Wipf P, Tzounopoulos T (2016) Synthesis and evaluation of potent KCNQ2/3-specific channel activators. Mol Pharmacol 89:667–677.

Li S, Choi V, Tzounopoulos T (2013) Pathogenic plasticity of Kv7.2/3 channel activity is essential for the induction of tinnitus. Proc Natl Acad Sci USA 110:9980–9985.

Li S, Kalappa BI, Tzounopoulos T (2015) Noise-induced plasticity of KCNQ2/3 and HCN channels underlies vulnerability and resilience to tinnitus. Elife 4:e07242.

Liu R, Tzounopoulos T, Wipf P (2019) Synthesis and optimization of Kv7 (KCNQ) potassium channel agonists: the role of fluorines in potency and selectivity. ACS Med Chem Lett 10:929–935.

Manville RW, Abbott GW (2018) Gabapentin is a potent activator of KCNQ3 and KCNQ5 potassium channels. Mol Pharmacol 94:1155–1163.

Mataga N, Mizuguchi Y, Hensch TK (2004) Experience-dependent pruning of dendritic spines in visual cortex by tissue plasminogen activator. Neuron 44:1031–1041.

Merzenich MM, Kaas JH, Wall J, Nelson RJ, Sur M, Felleman D (1983) Topographic reorganization of somatosensory cortical areas 3b and 1 in adult monkeys following restricted deafferentation. Neuroscience 8:33–55.

Metherate R, Aramakis VB (1999) Intrinsic electrophysiology of neurons in thalamorecipient layers of developing rat auditory cortex. Brain Res Dev Brain Res 115:131–144.

Miceli F, Soldovieri MV, Ambrosino P, Manocchio L, Mosca I, Taglialatela M (2018) Pharmacological targeting of neuronal Kv7.2/3 channels: a focus on chemotypes and receptor sites. Curr Med Chem 25:2637–2660.

Miyamae T, Chen K, Lewis DA, Gonzalez-Burgos G (2017) Distinct physiological maturation of parvalbumin-positive neuron subtypes in mouse prefrontal cortex. J Neurosci 37:4883–4902.

Moore AK, Weible AP, Balmer TS, Trussell LO, Wehr M (2018) Rapid rebalancing of excitation and inhibition by cortical circuitry. Neuron 97:1341–1355.e6.

Ostacolo C, Miceli F, Di Sarno V, Nappi P, Iraci N, Soldovieri MV, Ciaglia T, Ambrosino P, Vestuto V, Lauritano A, Musella S, Pepe G, Basilicata MG, Manfra M, Perinelli DR, Novellino E, Bertamino A, Gomez-Monterrey IM, Campiglia P, Taglialatela M (2020) Synthesis and pharmacological characterization of conformationally restricted retigabine analogues as novel neuronal Kv7 channel activators. J Med Chem 63:163–185.

Oswald AM, Reyes AD (2008) Maturation of intrinsic and synaptic properties of layer 2/3 pyramidal neurons in mouse auditory cortex. J Neurophysiol 99:2998–3008.

Oyrer J, Maljevic S, Scheffer IE, Berkovic SF, Petrou S, Reid CA (2018) Ion channels in genetic epilepsy: from genes and mechanisms to disease-targeted therapies. Pharmacol Rev 70:142–173.

Persic D, Thomas ME, Pelekanos V, Ryugo DK, Takesian AE, Krumbholz K, Pyott SJ (2020) Regulation of auditory plasticity during critical periods and following hearing loss. Hear Res 397:107976.

Qiu C, Salvi R, Ding D, Burkard R (2000) Inner hair cell loss leads to enhanced response amplitudes in auditory cortex of unanesthetized chinchillas: evidence for increased system gain. Hear Res 139:153–171.

Rasmusson DD (1982) Reorganization of raccoon somatosensory cortex following removal of the fifth digit. J Comp Neurol 205:313–326.

Resnik J, Polley DB (2017) Fast-spiking GABA circuit dynamics in the auditory cortex predict recovery of sensory processing following peripheral nerve damage. Elife 6:e21452.

Resnik J, Polley DB (2021) Cochlear neural degeneration disrupts hearing in background noise by increasing auditory cortex internal noise. Neuron 109:984–996.e4.

Robertson D, Irvine DR (1989) Plasticity of frequency organization in auditory cortex of guinea pigs with partial unilateral deafness. J Comp Neurol 282:456–471.

Rock C, Zurita H, Lebby S, Wilson CJ, Apicella AJ (2018) Cortical circuits of callosal GABAergic neurons. Cereb Cortex 28:1154–1167.

Ruebhausen MR, Brozoski TJ, Bauer CA (2012) A comparison of the effects of isoflurane and ketamine anesthesia on auditory brainstem response (ABR) thresholds in rats. Hear Res 287:25–29.

Sarro EC, Kotak VC, Sanes DH, Aoki C (2008) Hearing loss alters the subcellular distribution of presynaptic GAD and postsynaptic GABAA receptors in the auditory cortex. Cereb Cortex 18:2855–2867.

Scholl B, Wehr M (2008) Disruption of balanced cortical excitation and inhibition by acoustic trauma. J Neurophysiol 100:646–656.

Seefeld MA, et al. (2018) Novel K(V)7 ion channel openers for the treatment of epilepsy and implications for detrusor tissue contraction. Bioorg Med Chem Lett 28:3793–3797.

Seki S, Eggermont JJ (2003) Changes in spontaneous firing rate and neural synchrony in cat primary auditory cortex after localized tone-induced hearing loss. Hear Res 180:28–38.

Soh H, Park S, Ryan K, Springer K, Maheshwari A, Tzingounis AV (2018) Deletion of KCNQ2/3 potassium channels from PV$^+$ interneurons leads to homeostatic potentiation of excitatory transmission. Elife 7:e38617.

Soldovieri MV, Miceli F, Taglialatela M (2011) Driving with no brakes: molecular pathophysiology of Kv7 potassium channels. Physiology (Bethesda) 26:365–376.

Song P, Yang Y, Barnes-Davies M, Bhattacharjee A, Hamann M, Forsythe ID, Oliver DL, Kaczmarek LK (2005) Acoustic environment determines phosphorylation state of the Kv3.1 potassium channel in auditory neurons. Nat Neurosci 8:1335–1342.

Strumbos JG, Polley DB, Kaczmarek LK (2010) Specific and rapid effects of acoustic stimulation on the tonotopic distribution of Kv3.1b potassium channels in the adult rat. Neuroscience 167:567–572.

Sun QQ (2009) Experience-dependent intrinsic plasticity in interneurons of barrel cortex layer IV. J Neurophysiol 102:2955–2973.

Takesian AE, Hensch TK (2013) Balancing plasticity/stability across brain development. Prog Brain Res 207:3–34.

Takesian AE, Kotak VC, Sharma N, Sanes DH (2013) Hearing loss differentially affects thalamic drive to two cortical interneuron subtypes. J Neurophysiol 110:999–1008.

Takesian AE, Bogart LJ, Lichtman JW, Hensch TK (2018) Inhibitory circuit gating of auditory critical-period plasticity. Nat Neurosci 21:218–227.

Tatulian L, Delmas P, Abogadie FC, Brown DA (2001) Activation of expressed KCNQ potassium currents and native neuronal M-type potassium currents by the anti-convulsant drug retigabine. J Neurosci 21:5535–5545.

Thiele N, Köppl C (2018) Gas anesthesia impairs peripheral auditory sensitivity in barn owls (*Tyto alba*). eNeuro 5:ENEURO.0140-18.2018.

Tremblay R, Lee S, Rudy B (2016) GABAergic interneurons in the neocortex: from cellular properties to circuits. Neuron 91:260–292.

Tzounopoulos T, Balaban C, Zitelli L, Palmer C (2019) Towards a mechanistic-driven precision medicine approach for tinnitus. J Assoc Res Otolaryngol 20:115–131.

Vale C, Schoorlemmer J, Sanes DH (2003) Deafness disrupts chloride transporter function and inhibitory synaptic transmission. J Neurosci 23:7516–7524.

Vigil FA, Carver CM, Shapiro MS (2020) Pharmacological manipulation of K (v) 7 channels as a new therapeutic tool for multiple brain disorders. Front Physiol 11:688.

Wang W, Zhang LS, Zinsmaier AK, Patterson G, Leptich EJ, Shoemaker SL, Yatskievych TA, Gibboni R, Pace E, Luo H, Zhang J, Yang S, Bao S (2019) Neuroinflammation mediates noise-induced synaptic imbalance and tinnitus in rodent models. PLoS Biol 17:e3000307.

Wang W, Deng D, Jenkins K, Zinsmaier AK, Zhou Q, Bao S (2022) Correlation of electrophysiological and gene transcriptional dysfunctions in single cortical parvalbumin neurons after noise trauma. Neuroscience 482:87–99.

Wang X (2016) The ying and yang of auditory nerve damage. Neuron 89:680–682.

Wu J, Kaczmarek LK (2021) Modulation of neuronal potassium channels during auditory processing. Front Neurosci 15:596478.

Xia D, Zhang X, Deng D, Ma X, Masri S, Wang J, Bao S, Hu S, Zhou Q (2021) Long-term enhancement of NMDA receptor function in inhibitory neurons preferentially modulates potassium channels and cell adhesion molecules. Front Pharmacol 12:796179.

Xiong Q, Sun H, Zhang Y, Nan F, Li M (2008) Combinatorial augmentation of voltage-gated KCNQ potassium channels by chemical openers. Proc Natl Acad Sci USA 105:3128–3133.

Yang S, Weiner BD, Zhang LS, Cho SJ, Bao S (2011) Homeostatic plasticity drives tinnitus perception in an animal model. Proc Natl Acad Sci USA 108:14974–14979.

Yang S, Su W, Bao S (2012) Long-term, but not transient, threshold shifts alter the morphology and increase the excitability of cortical pyramidal neurons. J Neurophysiol 108:1567–1574.

Ye W, Zhao H, Dai Y, Wang Y, Lo YH, Jan LY, Lee CH (2022) Activation and closed-state inactivation mechanisms of the human voltage-gated K (V)4 channel complexes. Mol Cell 82:2427–2442.e4.

Zhang F, Liu Y, Tang F, Liang B, Chen H, Zhang H, Wang K (2019) Electrophysiological and pharmacological characterization of a novel and potent neuronal Kv7 channel opener SCR2682 for antiepilepsy. FASEB J 33:9154–9166.